SUPPLEMENTARY INFORMATION

Alcohol Dependence Modifies Brain Networks Activated During Withdrawal and Reaccess: A C-fos-based Analysis in Mice

Roland *et al.*

Methods

Subjects

For CIE/FSS studies, male C57BL/6J mice (10 weeks of age) were obtained from Jackson Laboratories (Bar Harbor, ME). For chemogenetic experiments, 7-week-old male C57BL/6J mice were obtained in-house from the University of North Carolina. All mice were individually housed, maintained on a 12-h reverse light/dark cycle, and provided free access to food and water throughout the duration of the experiments. CIE/FSS and brain tissue harvest protocols were approved by the Medical University of South Carolina Institutional Animal Care and Use Committee. Follow-up CIE and chemogenetic studies were approved by the Institutional Animal Care and Use Committee of the University of North Carolina. All experiments were consistent with guidelines of the NIH Guide for the Care and Use of Laboratory Animals.

Chronic intermittent ethanol exposure

During a 6-week baseline drinking period, mice had access to a bottle containing alcohol (15% v/v) for 1 h daily (M-F) beginning 4h into the dark cycle. Mice were then divided into two groups based on the average intake in the final baseline week. Mice were exposed to either room air (AIR) or alcohol vapor (CIE) for four consecutive days (16 h on/8 h off) on alternating weeks, with interleaved test drinking weeks. Blood was collected from the retroorbital sinus (MUSC studies)

or tail (UNC studies) once during each vapor week for determination of blood ethanol content (BEC) using an Analox AM1 Analyser (Analox Instruments, UK). During test drinking weeks, mice had daily (M-F) 1h access to alcohol to assess voluntary consumption.

Forced swim stress

During intermittent voluntary drinking weeks, subgroups of AIR and CIE mice underwent forced swim stress four hours prior to each drinking session as previously described (1,2). Briefly, mice were placed into a glass cylinder containing 23–25° C water at a depth of 20 cm for 10 minutes. Mice were placed back into their home cage, which was situated on a heated pad, for 5 minutes, and then returned to the colony room. Glass cylinders were cleaned between subjects and nonstressed mice remained in their home cages for the duration.

Brain Tissue Collection

Following the fourth alcohol vapor cycle, mice were provided 1h access to alcohol on days 1 and 2 of test 4. On day 3, FSS groups underwent forced swim stress, and 5h later a subgroup of mice from all treatment groups were deeply anesthetized with urethane (1.5 mg/kg i.p.) and transcardially perfused with 10 mL PBS followed by 10 mL 4% paraformaldehyde (PFA) in phosphate buffered saline (PBS). The remaining mice were provided 1h access to alcohol and perfused 1h after termination of the drinking session. Brains were immediately extracted following perfusion, post-fixed for 24 h at 4C in 4% PFA, and transferred to PBS for long-term storage prior to immunostaining.

iDISCO whole-brain immunostaining

Brains were hemisected approximately 1 mm lateral to the midline, and left and right hemispheres were collected alternately. Whole-brain immunostaining for c-fos was performed according to published methods (3). Briefly, hemisected brains were dehydrated in a series of 20%, 40%, 60%,

80%, and 100% methanol in ddH$_2$O (1h each). Brains were bleached overnight in 5% hydrogen peroxide in methanol, then rehydrated in a reverse series of 100-20% methanol in ddH$_2$O. Following three washes in PBS, brains were washed in PBS/0.2%Triton-X-100, permeabilized for 2 days at 37C in a solution containing 0.3M glycine and 20% DMSO in PBS/0.2% Triton-X-100, blocked for 2 days at 37C in PBS/0.2% Triton-X-100/10% DMSO/6% donkey serum, and incubated for 7 days in primary antibody (rabbit anti-cFos, 1:2000; Synaptic Systems #226-003) in PBS/0.2% Tween-20/10% DMSO/6% donkey serum and 10 ug/mL heparin. Following a wash step in PBS/0.2% Tween-20/heparin, brains were incubated in secondary antibody (donkey anti-rabbit Alexa Fluor 647, Thermo Fisher Scientific #A-31573) at 1:500 in PBS/0.2% Tween-20/10% DMSO/6% donkey serum/heparin for 7 days. Brains were washed again with PBS/0.2% Tween-20/heparin, then dehydrated a second time in a decreasing series of 20-100% methanol in PBS as above. The next day, brains were incubated in a solution of 66% dichloromethane/33% methanol for three hours, then two consecutive times in 100% DCM for 15 min each. After incubation in DCM, brains were transferred to a clean tube containing dibenzyl ether until imaging.

Light sheet imaging

Cleared brain hemispheres were imaged in the sagittal orientation using a light sheet microscope (Ultramicroscope II, LaVision Biotec, Bielefeld, Germany) with an Olympus MVPLAPO 2X/0.5 objective and an Andor Zyla 5.5 camera. The dorsal surface of the brain was oriented closest to the light sheet, and images were collected using ImspectorPro software. Scans were performed using three angled light sheets, a light sheet numerical aperture of 0.026, sheet width of 100%, and Z step of 6 um. Brains were imaged in the 488 nm channel at 0.8x magnification for detection of autofluorescence as a single Z stack. The 647 nm channel was imaged at 2x magnification to image c-fos stained nuclei in 35-48 tiles (adjusted based on sample size). The field of view was cropped to 1000 x 1000 pixels, and stacks were acquired with a 10% overlap in X and Y. In a separate image processing step, tiled images were aligned using the Imaris Stitcher.

ClearMap Analysis

Open source ClearMap 1.0 software was used to analyze c-Fos-positive cell counts across brain regions using previously described methods (3). The scripts were implemented in Python 2.7 on a Dell Precision Tower 5810 running Ubuntu 16.04 LTS. Cell detection parameters included cell shape parameter threshold set to 8 pixels in diameter, and Difference of Gaussian smoothing was performed using a kernel of 8 x 8 x 4 voxels. Detected cells were registered to the Allen Brain Atlas 25 µm map using 3D transformation between the 647 and 488 channels, and the 488 channel and the Allen Brain Atlas map, in order to compute c-fos-positive cell counts for each region.

Functional network construction

We used the c-fos-positive cell counts to compute the between-subjects Pearson correlation coefficient *r* for all pairs of brain regions (110 regions) and defined it as our measure of coactivation. Because thresholding is arbitrary and may introduce biases such as false negatives and network density differences that skew group comparisons (4–6), and bias from data acquisition artifacts can cause false strong correlations, we chose not to apply thresholds. For each condition, we defined the adjacency matrix as the full correlation matrix, with the *r* coefficients as weights between each pair of regions. This resulted in signed (positive and negative), undirected and weighted networks representing the neural state of each condition. Each node in the network was labeled with its anatomical group according to the Allen Brain Atlas.

Network comparisons

To compare network properties among the four treatment groups (LD withdrawal, LD reaccess, HD withdrawal, HD reaccess), for each metric of interest we computed the empirical difference D^{emp} between groups and built a null model via a permutation procedure. First, we shuffled the

condition labels among subjects without replacement, reconstructed the networks, and calculated the metrics and their condition difference D^{null} under the random null hypothesis. If the metric was community-based, we used the empirical community partitions in the null model networks. We built a null model distribution based on 10000 permutations. Finally, we calculated a p value for each comparison, defined as the proportion of the D^{null} distribution that can explain D^{emp}, $p = (D^{emp} – D^{null}) / N -1$, where N = 10000. The level of significance for each comparison was α = 0.05, and FDR correction of the p value was performed in nodal level comparisons.

Community detection and global metrics

Many network properties arise from the configuration of nodes into complex network-wide interaction patterns, described as communities, clusters, or modules. To capture community structures, we used a pipeline largely developed by a previous study on multiscale hierarchical consensus clustering (HCC) (11). We computed three global level metrics for each network: mean coactivation (mean r); anatomy-based modularity, which is the modularity quality function calculated using the anatomical groups for the community partition; and community-based modularity, calculated from the finest partition of the HCC procedure. We compared these metrics among the four treatment groups. To identify changes in the position of importance of individual brain regions among treatment conditions, and to examine how interactivity with other regions contributed to these changes, we computed two metrics to capture the position of a node within its network: within-community strength (wcs) and the diversity coefficient (h).

Multi-resolution Modularity – The modularity quality function measures the strength of 'clustering' in a network, given a community assignment vector $\vec{g}$, where g_i is the cluster containing the node *i*. Most community detection algorithms are based on modularity function optimization. The modularity quality function used in this study was built from the Reichart and Bornholdt (7) version of the modularity quality function,

5

$$Q(\vec{g}, \gamma) = \sum_{i,j=1}^{n} \left(A_{ij} - \gamma P_{ij} \right) \delta(g_i, g_j), \tag{1}$$

where A is the adjacency matrix, P is the expected adjacency matrix under a null model, γ is the resolution pair parameter, and δ (g_i, g_j) is the community co-assignment matrix, where δ = 1 if g_i = g_j, and δ = 0 otherwise. The resolution parameter influences the size of the clusters and can be tuned to encompass different scales. When applying the community detection algorithm in the empirical networks (see algorithm section below), we used the following typical null model (8),

$$P_{ij} = \frac{k_i k_j}{v}, \tag{2}$$

where k is the sum of all correlations of a given node, and v is the sum of all k values. We use this null model when applying the community detection algorithm in the empirical networks.

In this study, we used a variant of the modularity quality function, Q*, previously observed to be well-suited for correlation-based networks (9),

$$Q^* = Q^+ + \frac{v^-}{v^- v^+} Q^- \tag{3}$$

The modularity variant Q* assumes an unequal importance to the positive and negative correlations and provides the negative correlations a lower weight, proportional to their presence, such that if a network has equal numbers of positive and negative correlations, the contribution of positive correlations is twice that of negative.

Community detection algorithm – We used a Louvain-like algorithm for signed networks adapted from the community_louvain.m function in the Brain Connectivity Toolbox (https://sites.google.com/site/bctnet/). The Louvain algorithm is a heuristic based on maximizing the modularity quality function. It starts by selecting random nodes, grouping them locally into small communities if that increases modularity, then treating the small community as a node and repeating until there is no further increase in modularity (9,10).

Resolution parameter – The resolution parameter γ in (1) influences the null model P such that it tunes the size of the communities detected. It works as an inverted tuning knob in which increasing γ will tend to detect smaller communities. This effectively allows the detection of communities at different scales in the network, varying from a coarse scale with large communities (or no community at all) to the finest scale in which nodes are singleton communities. We adopted a multi-resolution approach that covers that range. However, when applying community detection until all nodes are singleton communities, certain correlations need values of γ scales of magnitude higher than most correlations to be separated, which can potentially make a linear or exponential selection of γ values to cover the whole range a costly approach. To circumvent this, we implemented a strategy used previously (11,12) to both determine the [γ_{min}, γ_{max}] range and sample meaningful γ values within this range (values that result in a change of community detection). Briefly, the [γ_{min}, γ_{max}] range was determined such that γ_{min} was the largest γ where no communities were detected, and γ_{max} was the smallest γ where all nodes are singleton communities. We calculated γ_{max} as the smallest γ such that $A_{ij} - P_{ij} \leq 0$ for all i and j. As in Jeub et al., we determined γ_{min} iteratively by first estimating γ_{min} using a small sample of partitions (20) at γ = 1, then sampled a new set of partitions using γ = $\gamma_{min} - \varepsilon$, where ε is a small constant (1^{-10}) that ensures γ_{min} is sub-optimal, then use the new sample to update γ_{min}. This procedure was repeated until the new sample consisted of only trivial partitions (no communities; for more details, see Jeub et al., 2018).

To sample γ values within the [γ_{min}, γ_{max}] range, we split the contributions of node pairs to modularity into ferromagnetic correlations $E^+(\gamma) = \{(i, j) \mid i \neq j, A_{ij} - \gamma P_{ij} > 0\}$ and antiferromagnetic correlations $E^-(\gamma) = \{(i, j) \mid i \neq j, A_{ij} - \gamma P_{ij} < 0\}$. Note that changing the γ value will change the correlations that become antiferromagnetic. As proposed by Jeub, we used the relative magnitude of the antiferromagnetic correlations as a measure of scales,

$$\beta(\gamma) = \frac{\sum_{(i,j)\in E^-(\gamma)} |A_{ij} - \gamma P_{ij}|}{\sum_{(i,j),i\neq j} |A_{ij} - \gamma P_{ij}|} \tag{4}$$

Note that when γ ≤ 0, β(γ) = 0, and when γ ≥ γ$_{max}$, β(γ) = 1, and β increases monotonically for 0 ≤ γ ≤ γ$_{max}$, that is, γ increases as a continuous variable, but β increases as if it were a discrete variable, changing when the "event" happens (i.e., the γ increases to a value that makes correlations become antiferromagnetic relative to before). We sampled β linearly between β$_{min}$ and β$_{max}$, given that β$_{min}$ = β(γ$_{min}$) and β$_{max}$ = β(γ$_{max}$). We then inverted the relationship between γ and β to calculate the γ sample,

$$\gamma(\beta) = \frac{\sum_{(i,j)\in E^-(\beta)} A_{ij} + \beta \left(\sum_{(i,j)\in E^-(\beta)} A_{ij} - \sum_{(i,j)\in E^-(\beta)} A_{ij} \right)}{\sum_{(i,j)\in E^-(\beta)} P_{ij} + \beta \left(\sum_{(i,j)\in E^-(\beta)} P_{ij} - \sum_{(i,j)\in E^-(\beta)} P_{ij} \right)} \tag{5}$$

Consensus Clustering – Community detection algorithms based on modularity maximization suffer from degeneracy, that is, multiple near-optimal results. When applying these algorithms in a network repeatedly, outputs with a degree of difference are expected. Consensus clustering is a recursive procedure that uses this inherent variation to define the degree of agreement of these near-optimal solutions and work with it in order to reach a more meaningful network partition (13,14).

The basis of consensus clustering implementation is the co-classification matrix C$_{ij}$, an *i x j matrix* where entries are the proportion each node pair is assigned to a same community t, given a set of partitions g,

$$C_{ij}(g) = \frac{1}{g}\sum\delta\left(g_i(t), g_j(t)\right). \tag{6}$$

We computed our co-classification matrices based on 1000 partitions using the γ range described above. In the co-classification matrix, values of 1 or 0 reflect the consensus that a given node pair always or never belong in the same community, respectively. The consensus clustering treats the co-classification matrix as a new network to find a consensus for all other values. One approach

to find consensus is to apply a threshold to the weights and all values below it to zero (15). Another approach is to build a null model based on the co-classification distribution and incorporate it in the calculation of P in the modularity quality function (11,16). Here, we adopted this procedure as proposed by Jeub et al. (2018), which uses the modularity quality function to perform a hypothesis test

$$Q_C(\vec{g}, \alpha) = \sum \left(C_{ij} - P_{ij}^{null}(\alpha) \right) \delta(g_i, g_j), \tag{7}$$

where α is the significance level, and P_{ij}null(α) is the highest value between the expected probability of *i* belonging to the same community of *j* and vice-versa (see *Null Model* below). In this hypothesis test, pairs of nodes that co-occur significantly less than can be explained by the null matrix P_{ij}null contribute negatively to the equation in (7) and are separated (see Jeub et al., 2018 for more details).

In order to obtain a consensus partition, we used an iterative procedure (15). The sequence of obtaining a set of partitions with the Louvain algorithm, calculating the co-classification matrix and identifying the links between communities with equation (7) was repeated until the co-classification matrix was binary, that is, until there was consensus as to which nodes co-occurred in the same community and which did not.

Null Model – We adopted a local permutation procedure to derive a co-classification matrix under the null model. A full description and rationale for the local permutation procedure can be found in the original publication (11). Briefly, after we obtained a set of 1000 partitions $\vec{g}$ from the signed Louvain-like algorithm (the same used to compute co-classification matrix), we fixed the community assignment of node *i* and permuted that of node *j*, keeping the number of communities and their size fixed, according to

$$P_{ij}^{null}(t) = Pr\left[g_j^0(t) = g_i(t) \vee g_i^0(t) = g_i(t)\right] = \frac{[\vec{g}(t) = g_i(t)] - 1}{n - 1}, \tag{8}$$

where $[\vec{g}(t) = g_i(t)]$ is the number of times node *i* is assigned to community *t*.

After the permutation procedure, we estimated the distribution and confidence intervals of the co-classification matrix under the null model using a pseudo-random sampling approximation at a level of significance of 0.05. Since this procedure keeps node *i* fixed and permutes node *j,* it assumes that $P_{ij}^{null} \neq P_{ji}^{null}$, for which we adopted the higher probability.

Hierarchical Consensus Clustering (HCC) – The consensus clustering procedure so far described the detection of communities at a single level. To fully assess all the levels of meaningful clustering in the networks, we made use of a recursive strategy proposed by (11). Briefly, once we detected the community structure at a given level, we treated each community as a network and repeated the procedure until no new communities were found at the significance level. This procedure generated a hierarchical clustering tree with multiple levels of significance.

After running HCC in the networks, we calculated the adjusted mutual information (AMI) between the final partition obtained from HCC or the anatomical groups partition and each partition of the partition distribution obtained using the γ range (Figure S1). We also show y(β) distribution used to compute those partitions (Figure S1).

All metrics were signed and normalized variants as suggested elsewhere (9). Briefly, given a node *i*, its strength *s* is defined as the sum of all connection weights in *i*, the within-community strength $s_i(g_i)$ is the strength of node *i* within its community g_i, and diversity coefficient is the normalized Shannon entropy of node *i* given its community g_i. We calculated the positive and negative contributions to normalized strength as

$$s_i'^{\pm} = \frac{s_i^{\pm}}{n-1},$$ (9)

Where *n* is the sum of the number of connections. The positive and negative contributions to normalized diversity coefficient were calculated as

$$h_i^\pm = -\frac{1}{log(max(g))} \sum_{g_i \in g} p_i^\pm(u) log p_i^\pm(u), \tag{10}$$

Where max(g) is the number of communities in the community partition g, $p(u) = \frac{s_i^\pm(g_i)}{s_i^\pm}$, where

$s_i^\pm(g_i)$ is the within-community strength of node i, given its community g_i. These normalized

metrics vary in the range of [0,1]. Finally, we normalized the metrics such that positive

contributions have more weight than negative,

$$s_i^* = s_i'^{+-}, \; h_i^* = h_i^{+-} \tag{11}$$

Both s_i^* and h_i^* have a [-1,1] range. Note that the normalizations shown above for strength were

applied to within-community strength, which was the metric used here. A detailed rationale about

the normalization can be found in the original proposal (9). The normalization allows a proper

comparison of our metrics between networks. We compared these metrics across the conditions

in our study as described above.

All network analysis was performed using R 4.0.2 (R Core Team, 2021) in Rstudio1.3.959

(RStudio Team, 2020), and the packages igraph (Csardi & Nepusz, 2006), boot (Canty & Ripley,

2020), data.tree (Glur, 2020), statGraph (da Costa et al., 2020), ggplot2 (Wickham, 2016), ggpubr

(Kassambara, 2020), pracma (Borchers, 2021), psych (Revelle, 2021) and custom codes

translated from Matlab from the Brain Connectivity Toolbox https://sites.google.com/site/bctnet/.

All the codes used in this study can be found

at https://github.com/coelhocao/Brain_Network_analysis.

Chemogenetic silencing of cortical amygdala neurons

8-week-old mice were stereotaxically injected with 200 nL AAV8-hSyn-hM4Di-mCherry or control

AAV8-hSyn-mCherry virus in bilateral COA (coordinates: -1.7 AP, +-2.8 ML, -5.9 DV). Because

c-fos counts were elevated in CIE mice in both anterior and posterior COA, we chose relatively

central injection coordinates that would allow viral diffusion to both subregions (17). Following a 2-week surgical recovery period, mice underwent 4-5 weeks of baseline drinking and 4 cycles of CIE as described above. Beginning in test 3, mice received daily i.p. saline injections 30 minutes prior to voluntary drinking sessions. On drinking day 3 of test 4, corresponding to the day of brain tissue harvest for iDISCO in the previous cohort, mice received an i.p. injection of 3 mg/kg CNO 30 minutes prior to drinking. The following week, sucrose preference tests were performed. Mice were given 2h access to either water 5% (w/v) sucrose solution for habituation on the first day. On the following two days, mice received an i.p. injection of either saline or 3 mg/kg CNO, and 30 min later were given 1h access to sucrose or water. One week after sucrose testing, locomotor activity was tested 30 min following a 3 mg/kg CNO injection using SuperFlex boxes (Omnitech Electronics, Accuscan, Columbus, OH). At the completion of all behavioral experiments, mice were perfused and brains extracted for verification of viral placement.

Data analysis

C-fos count data were analyzed by 2-way ANOVA and Tukey's post-hoc tests using R software. The level of significance for each comparison was $\alpha = 0.05$, and an FDR of 5% was applied to correct for multiple comparisons. For drinking experiments, fluid consumption was determined by weighing bottles before and after drinking sessions. An empty cage mounted with a bottle containing the indicated fluid (alcohol, water, or sucrose) was used to estimate weight loss due to fluid drip, and drinking values were corrected accordingly. Consumption was expressed as g/kg body weight (adjusted for respective fluid density). Drinking data and behavioral data were analyzed in Prism using 2-way or 3-way ANOVA followed by Tukey's or Sidak's post hoc testing as appropriate. Alpha was set at 0.05 for all comparisons.

Supplemental References

1. Anderson RI, Lopez MF, Becker HC (2016): Forced swim stress increases ethanol consumption in C57BL/6J mice with a history of chronic intermittent ethanol exposure. *Psychopharmacology (Berl)* 233: 2035–2043.

2. Lopez MF, Anderson RI, Becker HC (2016): Effect of different stressors on voluntary ethanol intake in ethanol-dependent and nondependent C57BL/6J mice. *Alcohol* 51: 17–23.

3. Renier N, Wu Z, Simon DJ, Yang J, Ariel P, Tessier-Lavigne M (2014): iDISCO: a simple, rapid method to immunolabel large tissue samples for volume imaging. *Cell* 159: 896–910.

4. Drakesmith M, Caeyenberghs K, Dutt A, Lewis G, David AS, Jones DK (2015): Overcoming the effects of false positives and threshold bias in graph theoretical analyses of neuroimaging data. *Neuroimage* 118: 313–333.

5. Langer N, Pedroni A, Jäncke L (2013): The problem of thresholding in small-world network analysis. *PLoS One* 8: e53199.

6. van den Heuvel MP, de Lange SC, Zalesky A, Seguin C, Yeo BTT, Schmidt R (2017): Proportional thresholding in resting-state fMRI functional connectivity networks and consequences for patient-control connectome studies: Issues and recommendations. *Neuroimage* 152: 437–449.

7. Reichardt J, Bornholdt S (2006): Statistical mechanics of community detection. *Phys Rev E Stat Nonlin Soft Matter Phys* 74: 016110.

8. Newman MEJ, Girvan M (2004): Finding and evaluating community structure in networks. *Phys Rev E Stat Nonlin Soft Matter Phys* 69: 026113.

9. Rubinov M, Sporns O (2011): Weight-conserving characterization of complex functional brain networks. *Neuroimage* 56: 2068–2079.

10. Blondel VD, Guillaume J-L, Hendrickx JM, de Kerchove C, Lambiotte R (2008): Local leaders in random networks. *Phys Rev E Stat Nonlin Soft Matter Phys* 77: 036114.

11. Jeub LGS, Sporns O, Fortunato S (2018): Multiresolution Consensus Clustering in Networks. *Sci Rep* 8: 3259.

12. Onnela J-P, Fenn DJ, Reid S, Porter MA, Mucha PJ, Fricker MD, Jones NS (2012): Taxonomies of networks from community structure. *Phys Rev E Stat Nonlin Soft Matter Phys* 86: 036104–036104.

13. Sporns O (2018): Graph theory methods: applications in brain networks. *Dialogues Clin Neurosci* 20: 111–121.

14. Sporns O, Betzel RF (2016): Modular Brain Networks. *Annu Rev Psychol* 67: 613–640.

15. Lancichinetti A, Fortunato S (2012): Consensus clustering in complex networks. *Sci Rep* 2: 336.

16. Betzel RF, Byrge L, Esfahlani FZ, Kennedy DP (2020): Temporal fluctuations in the brain's modular architecture during movie-watching. *Neuroimage* 213: 116687.

17. Root CM, Denny CA, Hen R, Axel R (2014): The participation of cortical amygdala in innate, odor-driven behavior. *Nature* 515: 269–273.

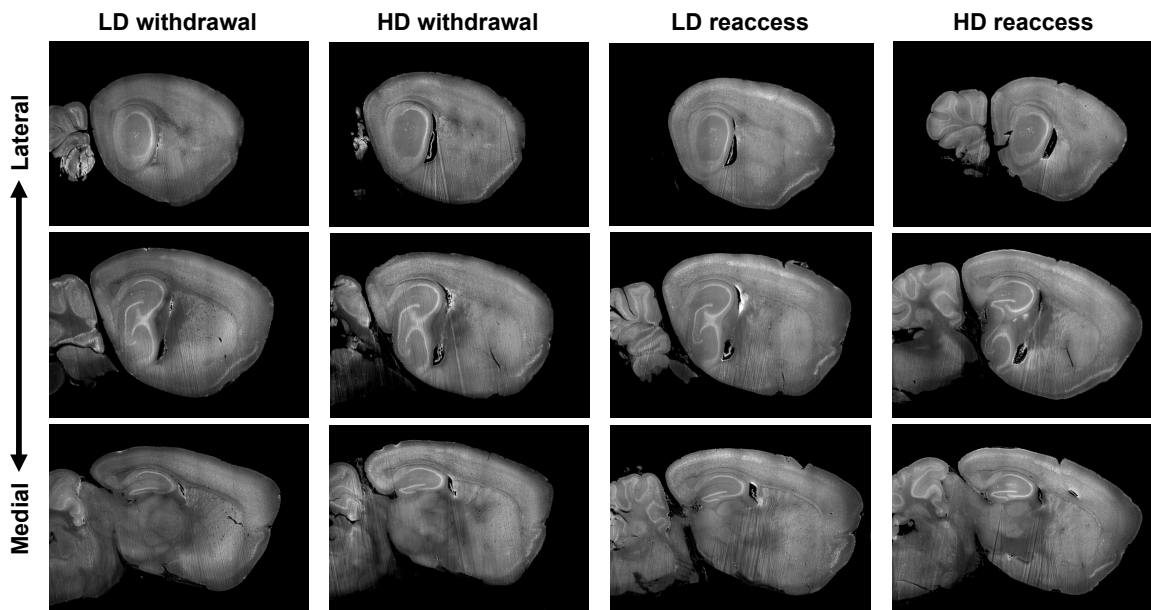**Supplemental Figures**

Figure S1.

Figure S1. Representative images of cleared brain hemispheres from low drinkers (LD) during withdrawal, high drinkers (HD) during withdrawal, LD after alcohol reaccess, and HD after alcohol reaccess. Representative images from lateral (top) to medial (bottom) are shown.
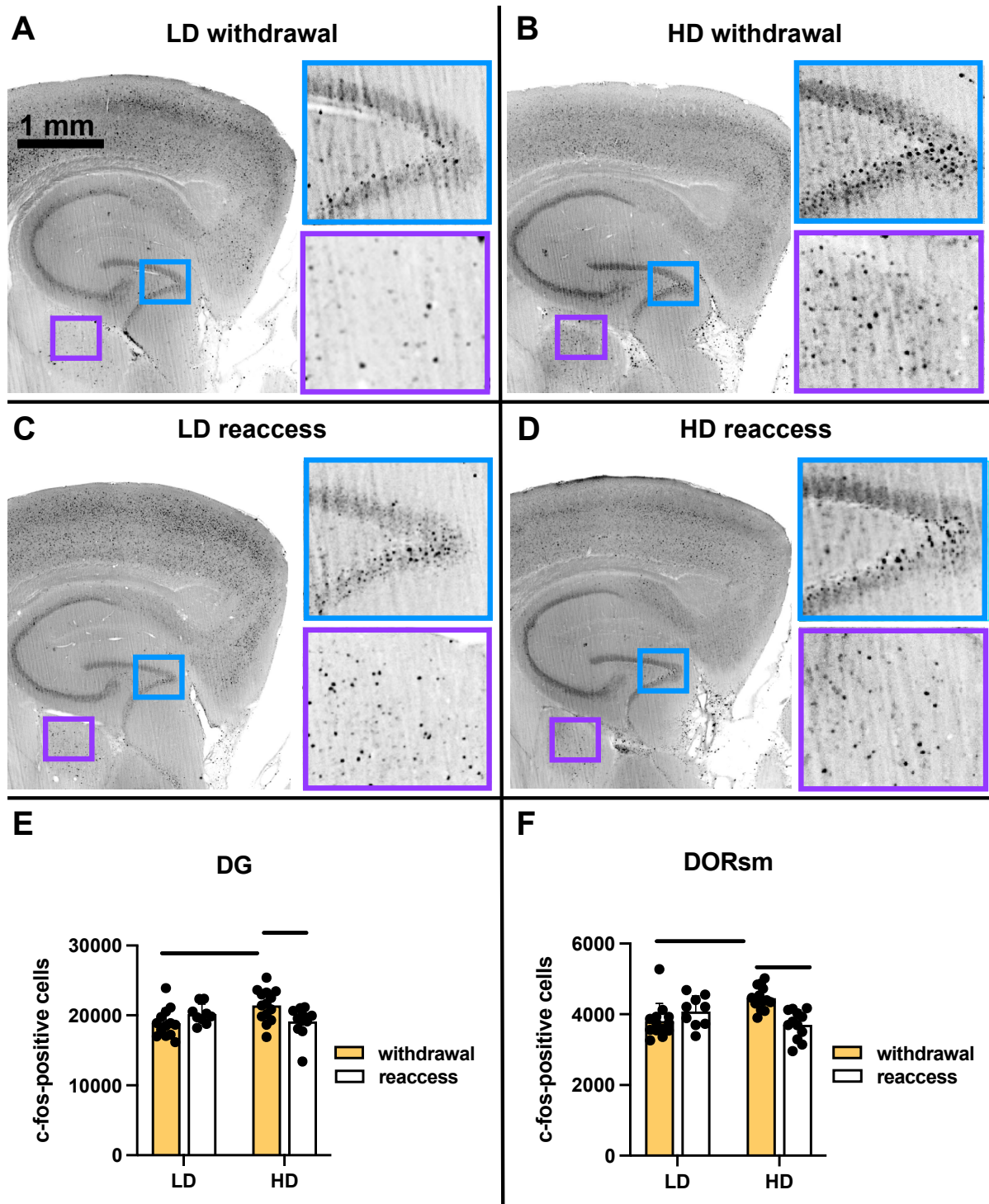
Figure S2.

Figure S2. A-D, Representative sagittal images of c-fos-stained brain tissue used for ClearMap automated cell detection in low-drinking (LD) and high-drinking (HD) mice during alcohol

withdrawal and following alcohol reaccess. Insets show higher magnification images of the dentate gyrus (DG, blue) and sensory-motor cortex related thalamus (DORsm, purple). E, Clearmap-generated cell counts for the DG for the four treatment groups. During withdrawal, HD mice showed higher c-fos expression in the DG relative to LD mice ($p < 0.05$). HD mice had lower c-fos expression in the DG following reaccess as compared to withdrawal ($p < 0.05$). F, Clearmap-generated cell counts for the DORsm for the four treatment groups. During withdrawal, HD mice showed higher c-fos expression in the DORsm relative to LD mice ($p < 0.01$). HD mice had lower c-fos expression in the DORsm following reaccess as compared to withdrawal ($p < 0.001$).
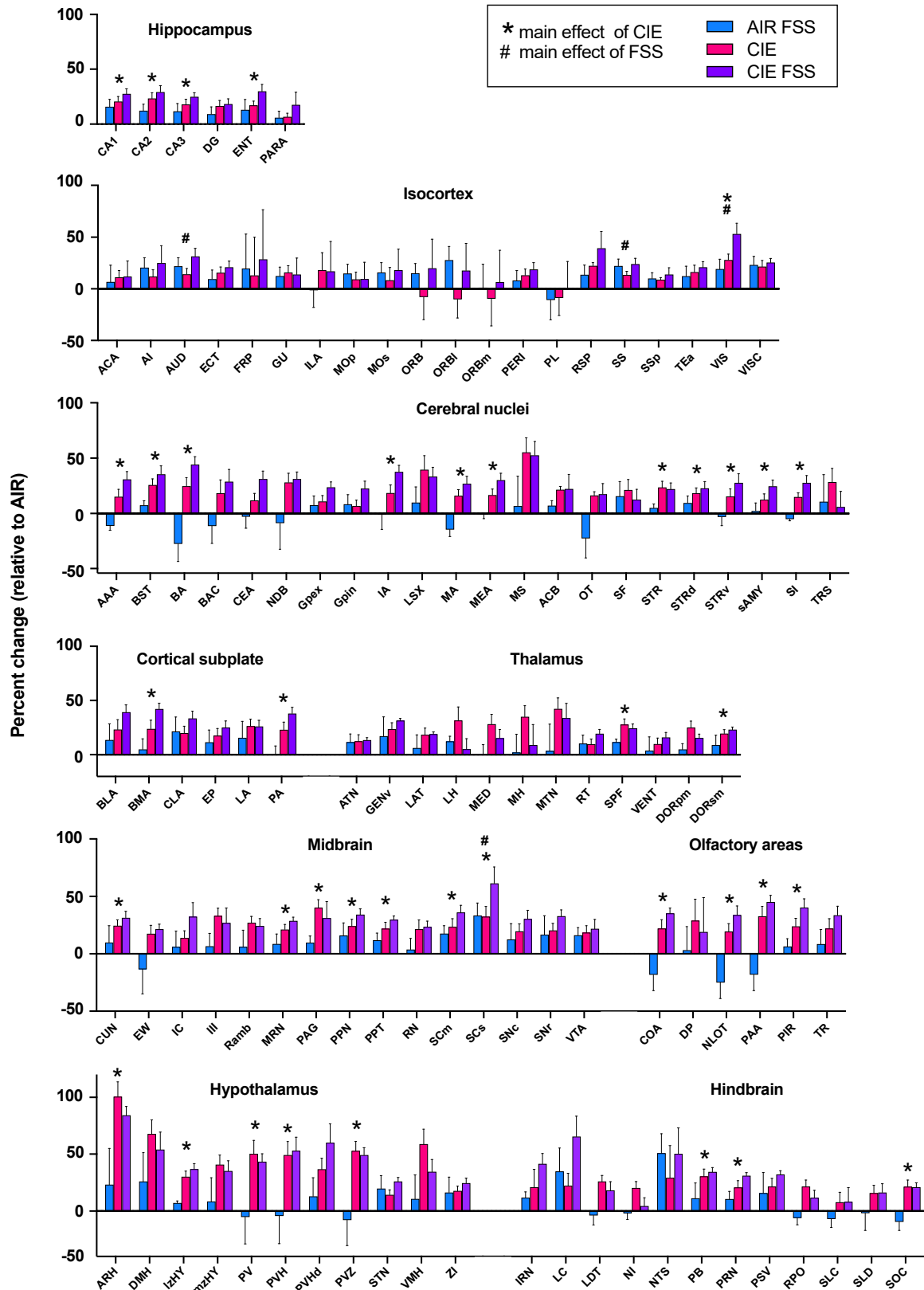
Figure S3.

Figure S3. Relative c-fos expression in CIE and/or FSS-exposed mice during acute (24 h) alcohol withdrawal. C-fos-positive cell counts are represented as the percent change relative to AIR mice for each region. Regions are grouped by anatomical subdivision according to the Allen Brain Atlas. * denotes a significant main effect of CIE; # denotes a significant main effect of FSS (2-way ANOVA with FDR correction for multiple comparisons). Post-hoc test p-values are available in Table S3.
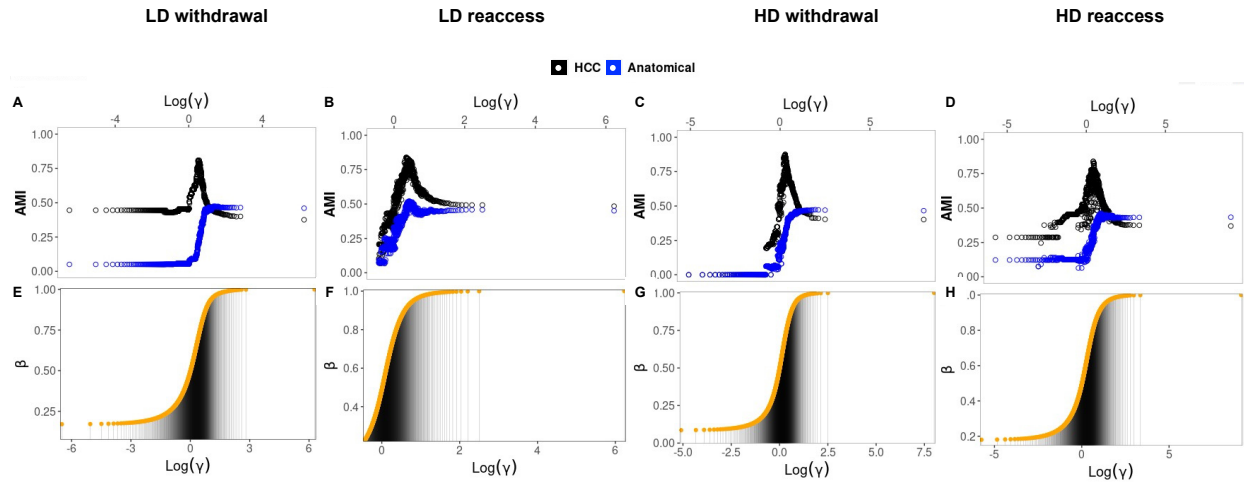
Figure S4.

Figure S4. A-D, The adjusted mutual information (AMI) between the partition distribution used in hierarchical consensus clustering (HCC) and the HCC finest partition (in black) or the anatomical groups partition (in blue) for low-drinking (LD) and high-drinking (HD) groups in the withdrawal and reaccess conditions. The AMI relative to the finest partition peaked at around 0.8 for the γ values that provided partitions closer to the finest HCC partition. The γ values at which the HCC finest partition peaked coincided with that at which the AMI relative to the anatomical groups partition also peaked, though at an AMI roughly around 0.5. Since AMI is an index where a value of zero means independence between the two variables compared, these AMI values indicate that the HCC community partition had a partial agreement with the anatomical groups. E-H, The γ(β) distribution for each group used to compute the partitions in A-D.